Received: 31 March 2022 | Revised: 16 November 2022 | Accepted: 2 December 2002

DOI: 10.1002/mp.16151

RESEARCH ARTICLE

MEDICAL PHYSICS

Technical performance of a dual-energy CT system with a novel deep-learning based reconstruction process: Evaluation using an abdomen protocol

Luuk J. Oostveen[1] | **Kirsten L. Boedeker**[2] | **Christiana Balta**[2] | **Daniel Shin**[3] | **Frank de Lange**[1] | **Mathias Prokop**[1] | **Ioannis Sechopoulos**[1,4]

[1]Department of Medical Imaging, Radboud University Medical Center, Nijmegen, The Netherlands

[2]Canon Medical Systems Corporation, Otawara, Japan

[3]Canon Medical Systems Europe, Zoetermeer, The Netherlands

[4]Technical Medicine Center, University of Twente, Enschede, The Netherlands

Correspondence
Luuk Oostveen, Radboud University Medical Center, Department of Medical Imaging, P.O. Box 9101 (route 766), 6500 HB Nijmegen, The Netherlands.
Email: Luuk.Oostveen@radboudumc.nl

Funding information
Canon Medical Systems Corporation

Abstract

Background: A new tube voltage-switching dual-energy (DE) CT system using a novel deep-learning based reconstruction process has been introduced. Characterizing the performance of this DE approach can help demonstrate its benefits and potential drawbacks.

Purpose: To evaluate the technical performance of a novel DECT system and compare it to that of standard single-kV CT and a rotate/rotate DECT, for abdominal imaging.

Methods: DE and single-kV images of four different phantoms were acquired on a kV-switching DECT system, and on a rotate/rotate DECT. The dose for the acquisitions of each phantom was set to that selected for the kV-switching DE mode by the automatic tube current modulation (ATCM) at manufacturer-recommended settings. The dose that the ATCM would have selected in single-kV mode was also recorded. Virtual monochromatic images (VMIs) from 40 to 130 keV, as well as iodine maps, were reconstructed from the DE data. Single-kV images, acquired at 120 kV, were reconstructed using body hybrid iterative reconstruction. All reconstructions were made at 0.5 mm section thickness. Task transfer functions (TTFs) were determined for a Teflon and LDPE rod. Noise magnitude (SD), and noise power spectrum (NPS) were calculated using 240 and 320 mm diameter water phantoms. Iodine quantification accuracy and contrast-to-noise ratios (CNRs) relative to water for 2, 5, 10, and 15 mg I/ml were determined using a multi-energy CT (MECT) phantom. Low-contrast visibility was determined and the presence of beam-hardening artifacts and inhomogeneities were evaluated.

Results: The TTFs of the kV-switching DE VMIs were higher than that of the single-kV images for Teflon (20% TTF: 6.8 lp/cm at 40 keV, 6.2 lp/cm for single-kV), while for LDPE the DE TTFs at 70 keV and above were equivalent or higher than the single-kV TTF. All TTFs of the kV-switching DECT were higher than for the rotate/rotate DECT. The SD was lowest in the 70 keV VMI (12.0 HU), which was lower than that of single-kV (18.3 HU). The average NPS frequency varied between 2.3 lp/cm and 4.2 lp/cm for the kV-switching VMIs and was 2.2 lp/cm for single-kV. The error in iodine quantification was at maximum 1 mg I/ml (at 5 mg I/ml). The highest CNR for all iodine concentrations was at 60 keV, 2.5 times higher than the CNR for single-kV. At 70–90 keV, the number of visible low contrast objects was comparable to that in single-kV, while other VMIs showed

fewer objects. At manufacturer-recommended ATCM settings, the $CTDI_{vol}$ for the DE acquisitions of the water and MECT phantoms were 12.6 and 15.4 mGy, respectively, and higher than that for single-kV. The 70 keV VMI had less severe beam hardening artifacts than single-kV images. Hyper- and hypo-dense blotches may appear in VMIs when object attenuation exceeds manufacturer recommended limits.

Conclusions: At manufacturer-recommended ATCM settings for abdominal imaging, this DE implementation results in higher $CTDI_{vol}$ compared to single-kV acquisitions. However, it can create sharper, lower noise VMIs with up to 2.5 times higher iodine CNR compared to single-kV images acquired at the same dose.

KEYWORDS
computed tomography, dual energy and spectral, technology assessment

1 | Introduction

In dual-energy CT applications, projection data is acquired with low and high energy spectra. Five different techniques to accomplish this are currently used clinically: dual X-ray sources, split filters, dual-layer detectors, fast tube voltage-switching, and recently also photon counting.[1–3] From the acquired projection data, material-specific images, for example, iodine maps, can be reconstructed. In addition, attenuation images for routine interpretation can be created by combining the information from the high and low energy data. One approach to form these images results in so-called virtual monochromatic images (VMIs). These VMIs are aimed to resemble images that would have resulted from acquisitions performed with a monochromatic X-ray beam of a user-selectable X-ray energy.[1,4]

Material decomposition of dual energy data can be performed using image-based methods or projection data-based methods. The advantage of an image-based method is that it does not need matching low- and high-energy projection data. However, using projection domain methods makes it possible to eliminate beam-hardening artifacts.[4] In the case of fast tube-voltage switching systems, when a view is measured in one location at low energy, no information is measured at that location with high energy, and vice-versa. This results in a sequence of gaps in the raw sinogram data that need to be filled to prevent view-limiting artifacts and to perform optimal projection domain material decomposition. A recently introduced DE system performs this sinogram completion using a deep learning approach.

The full reconstruction process from raw DE sinograms with gaps to the creation of the VMIs is shown in Figure 1. The first step uses a deep convolutional neural network (DCNN) that completes the low- and high-energy sinograms based on the opposite-energy view at the location of interest as well as on the neighboring views of the same energy. The labeled data used for the training of the DCNN was complete low- and high-energy sinograms acquired separately at both energies (Figure 2).

The material decomposition is performed in the projection domain to generate sinograms for the basis materials. Then, these sinograms are reconstructed using deep learning-based processing, similar to the method used for single-kV.[5,6] Finally, the VMIs are generated from these reconstructed material images. Unlike conventional reconstruction based solely on kernels differing for each body region, this reconstruction process relies on optimization of the hyperparameters of the underlying neural network for each body region. A number of abdomen applications have been shown to potentially benefit from DECT imaging. These include renal stone characterization, tumor treatment response evaluation, and liver fibrosis quantification, among others.[7–11]

The goal of this work is to perform a technical evaluation of this dual energy CT system that uses rapid tube voltage-switching with a deep-learning approach to complete the sinogram data. We decided to focus on a DE abdomen protocol, due to the number of potential clinical benefits in this region, in addition to being a region that has a high attenuation range. We hypothesized that this would be more challenging for the DE algorithm.

2 | MATERIALS AND METHODS

For this evaluation, iodine quantification measurements were performed in the iodine-specific images, while the noise properties, resolution, HU-value accuracy, contrast-to-noise ratio (CNR) of iodine and other materials, and low contrast visibility were measured using the VMIs. Finally, we studied artifacts within and outside the manufacturer-recommended imaging specifications. The manufacturer recommends scanning patients with a maximum BMI of 35, approximately a water equivalent diameter (WED) of 32 cm[12] and to avoid additional attenuating material in the field of view (FOV) (e.g., arms) than the patient's body, to prevent low number of quanta in all or some parts of the acquired sinograms.

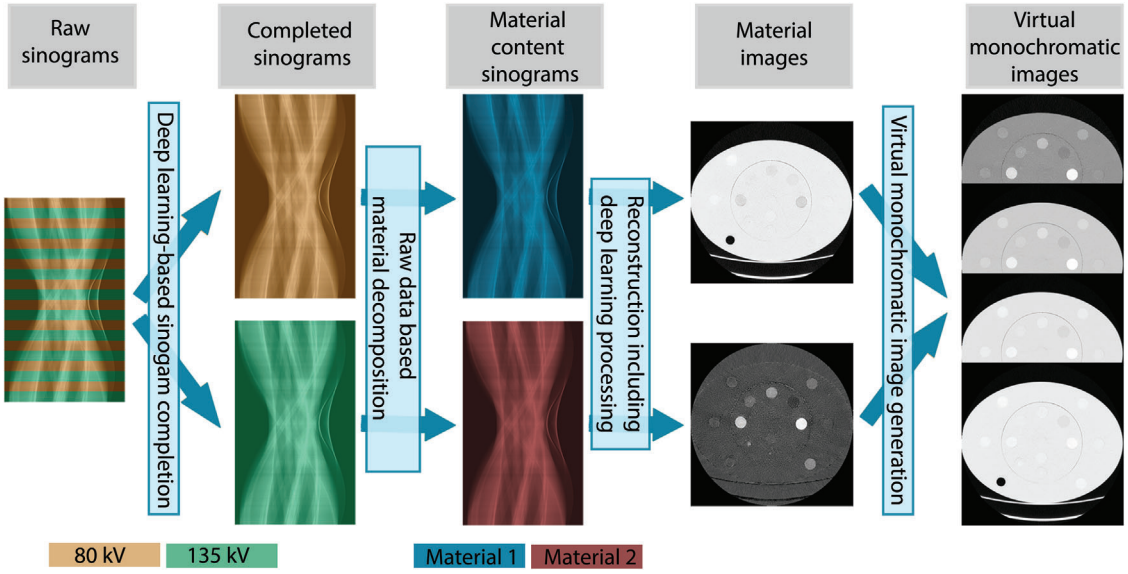

FIGURE 1 The full reconstruction path from raw sinograms with gaps to the generation of virtual monochromatic images. Deep learning-based methods are used for both sinogram completion and in the reconstruction from material content sinograms to material images

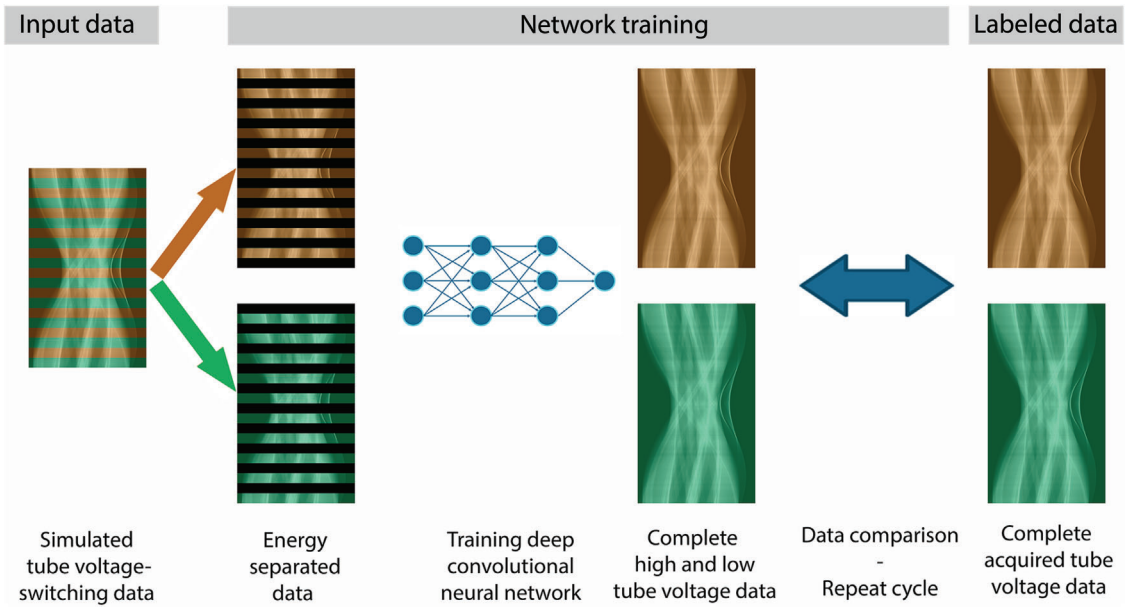

FIGURE 2 Graphical depiction of how the deep convolution neural network was trained to fill the gaps in the high and low energy sinogram data

2.1 | Phantoms

For the evaluation, five phantoms were used. Water phantoms with a diameter of 240 and 320 mm were used for characterizing the noise properties. The Catphan 500 phantom (The Phantom Laboratory, Greenwich, NY, USA) was used to determine the task transfer functions (TTFs) at different contrasts and the low-contrast visibility. The Multi-energy CT Phantom[13] (Sun Nuclear, Melbourne, Australia) was used to check the iodine concentration quantification, iodine CNR, and HU values. Finally, an Alderson Rando phantom (Radiology Support Devices, Carson, USA) was used to check for beam hardening artifacts in the pelvic region. Figure 3 shows a CT slice (single-kV acquisition) of these phantoms.

2.2 | CT acquisition and reconstruction

All acquisitions were performed on a 320 row-detector CT scanner (Aquilion ONE PRISM Edition, software version V10.4, Canon Medical Systems Corporation, Otawara, Japan). The phantoms were scanned using the

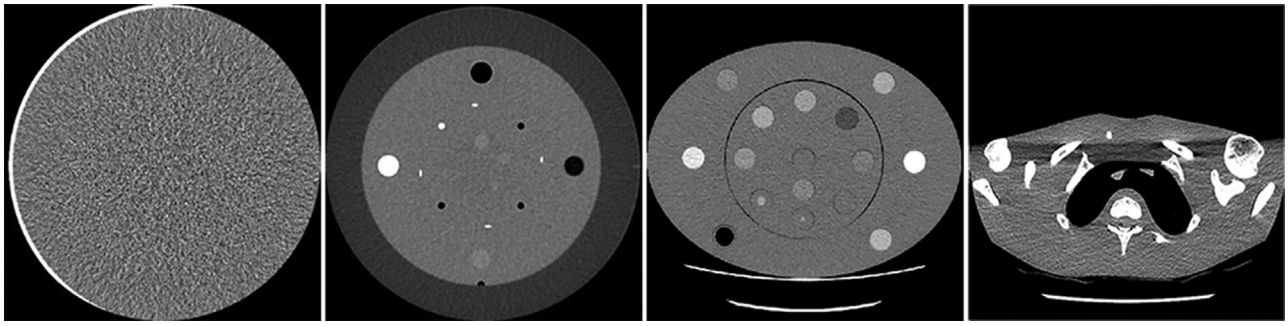

FIGURE 3 From left to right, CT images of the water phantom, the CTP401 module of the Catphan 500 containing Teflon and LDPE rods, the multi-energy CT (MECT) phantom containing rods of various materials and iodine concentrations, and the Alderson Rando phantom

TABLE 1 Parameters used for the acquisitions and reconstructions

Parameter	Dual energy (kV switching)	Single kV	Dual energy (rotate/rotate)
Tube voltage [kV]	80/135	120	80/135
Field of view [mm]	500	500	500
Tube current [mA]	Water/Catphan: 230[a] MECT: 280[a]	Water/Catphan: 200[b] MECT: 240[b]	Water/Catphan: 570/100[b] MECT: 630/110[b]
$CTDI_{vol}$ [mGy]	Water/Catphan: 12.6[a] MECT phantom: 15.4[a]	Water/Catphan: 12.6[b] MECT phantom: 15.2[b]	Water/Catphan: 12.6[b] MECT phantom: 15.2[b]
Rotation time [ms]	1000	1000	2 × 500
Collimation [mm]	80 × 0.5	80 × 0.5	80 × 0.5
Pitch	0.813	0.813	n.a. (axial)
Reconstruction			
TechniqueSection thickness[mm]	Spectral body 0.5	AIDR 3D enhanced, FC18 0.5	AIDR 3D enhanced, FC18 0.5

[a]Dual-energy tube current and $CTDI_{vol}$ for each phantom is based on the automatic exposure control with a setting of SD = 9 in DE mode.
[b]Single-energy tube current and DE rotate/rotate tube current are set to match the $CTDI_{vol}$ of the corresponding kV switching acquisitions.

manufacturer-default DE, kV switching, helical abdomen protocol with a one-second rotation time. Single-kV acquisitions were acquired at 120 kV and dose was matched based on the volume computed tomography dose index ($CTDI_{vol}$; Table 1). Single-kV reconstructions were performed using hybrid iterative reconstruction (Hybrid-IR, AIDR 3D enhanced, body-kernel: FC18). For DE, the reconstructions modes are based on anatomical regions rather than on kernels. For this study, focusing on abdomen, the "body" mode was chosen from the available anatomical regions. All DE reconstructions use the deep-learning based reconstruction method. For reference, DE acquisitions using a similar CT scanner (Aquilion ONE GENESIS Edition, Canon Medical Systems Corporation, Otawara, Japan) were also performed. On this scanner, DE acquisitions are performed using axial scans with two rotations; one using low tube voltage (80 kV) and one rotation with high tube voltage (135 kV). The images are reconstructed using Hybrid-IR (AIDR 3D enhanced, FC18). In this work, this DE method is referred to as "DE rotate/rotate." The dose was matched based on $CTDI_{vol}$.

VMIs from 40 to 130 keV, in 10 keV steps, as well as iodine maps, were reconstructed. For the kV-switching DECT this can be done on the CT itself, while for the DE rotate/rotate system the VMIs were created on a dedicated workstation (Vitrea, version 7.11, Canon Medical Systems Corporation).

2.3 | CT number and contrast to noise ratio

The manufacturer of the MECT phantom supplied attenuation coefficients for the rod materials from 40 to 200 keV, in 10 keV steps. The resulting HU values in the VMIs from rods containing air, adipose tissue, "solid water," 5 mg I/ml, 15 mg I/ml, and 300 mg Ca/ml were compared to the theoretical HU values calculated using the specified attenuation coefficients.

The mean HU value in each rod was measured within a circular region of interest (ROI) of 311 mm^2 (509 pixels) for 20 slices, each five slices apart. All ROI values within a rod were averaged and the standard deviation

(SD) was calculated. The average value was compared to the theoretical HU value for each VMI.

The same calculations were performed to determine the CNR to solid water of the rods containing various iodine concentrations (2, 5, 10, 15 mg I/ml), and the rods containing brain tissue, blood (electron density 1.03), adipose tissue, and air. CNR was calculated as $(HU_i - HU_w)/SD_w$, where HU_i is the average HU value within the rod, HU_w is the average HU value in the solid water rod, and SD_w is the SD in the solid water rod.

2.4 | Resolution

To determine the resolution, TTFs were calculated using the Teflon and LDPE rods in the CTP401 module of the Catphan 500 phantom, as described by Richard et al.[14] Briefly, first, for each reconstructed slice that contained the rod, the center of mass of the rod was located, and the edge spread function (ESF) was determined by averaging the pixel values at the same distance to the center of mass in bins of one-tenth of the pixel spacing. The average ESF was then determined by averaging the slice ESFs, from which the line spread function (LSF) was calculated by discrete differentiation. Finally, to obtain the TTF, the magnitude of the Fourier transform of the LSF was taken. The lowest frequency at which the TTF reaches 20% for each VMI was determined and compared to the results from the Hybrid-IR single-kV acquisitions and the DE rotate/rotate VMIs.

2.5 | Noise magnitude and texture

Noise texture was determined by calculating the noise power spectrum (NPS) for the various VMIs and single-kV reconstructions of the cylindrical 240 and 320 mm water phantoms. Reconstructions were made with a FOV of 320 mm. For each condition, 20 scans with an 8 cm scan range were acquired. Every fifth slice in each acquisition was used for the NPS calculation to improve statistics and prevent noise correlation between the slices. The radial profile of the 2D NPS was calculated from a 128 by 128 pixel ROI in the center of the slice.[15] As a single-parameter descriptor of the NPS, the average frequency of the radial profile was calculated. To quantify noise magnitude, SD were calculated in the ROIs that were used for the NPS calculation. The average of these SDs was used as a parameter to describe the noise magnitude.

2.6 | Iodine quantification

The estimates of the iodine concentrations in the iodine-containing rods in the MECT phantom were retrieved using a dedicated workstation (Vitrea, version 7.11, Canon Medical Systems Corporation) that determines the iodine concentrations based on the DE iodine images. The measured iodine concentrations were compared to the known iodine concentrations in the phantom (2, 5, 10, and 15 mg I/ml). The concentrations were estimated as the average within a circular ROI of 301 mm^2 (492 pixels) over 10 1 mm thick slices, each five slices apart.

2.7 | Low contrast visibility

One reader (LO), a clinical researcher with 23 years of experience in X-ray imaging, evaluated the middle slice of 10 mm thick reconstructions of the low contrast signal-module of the Catphan 500 phantom (module CTP515) using diagnostic monitors in a radiological reading room and determined the number of visible inserts for each contrast level in each VMI and in the single-kV reconstruction. The window width and window level of each image was adjusted to optimize the visibility of the low contrast objects in all images. The Catphan module contains inserts with low-contrast (1.0%, 0.5%, and 0.3%) being longer than 10 mm with a diameter ranging from 2 to 15 mm, resulting in nine supra-slice contrast inserts per contrast percentage. The module also contains inserts being shorter than 10 mm (7, 5, and 3 mm) with diameters from 3 to 9 mm, having 9 sub-slice contrast inserts in total.

2.8 | Artifacts

To compare the presence and magnitude of the beam hardening artifacts, images of the Alderson Rando phantom were compared visually. The phantom images were acquired using the manufacturer-recommended settings for the automatic tube current modulation (ATCM) (SD = 9 for DE, SD = 12.5 for Single-kV). The beam hardening artifacts were quantified using an artifact index (AI), defined as the difference in the mean HU value between a ROI placed inside the beam hardening artifact and that placed outside the artifact. In addition, the impact of having additional attenuating material in the FOV, adjacent to water phantoms with a diameter of 240 and 320 mm, was investigated to determine the effect of having imaging conditions beyond the manufacturer recommended imaging specifications.

2.9 | Dose comparison

The $CTDI_{vol}$ for DE was compared to the $CTDI_{vol}$ for single-kV acquisition at manufacturer-recommended settings. For this CT scanner, the noise index quality setting is set as a SD and therefore a higher number results in a lower dose. Settings for DE were the same as given in Table 1, except that instead of a fixed tube current a SD of 9 was set. For the single-kV acquisition, rotation time was set to 0.5 s, and SD was set at 12.5. The

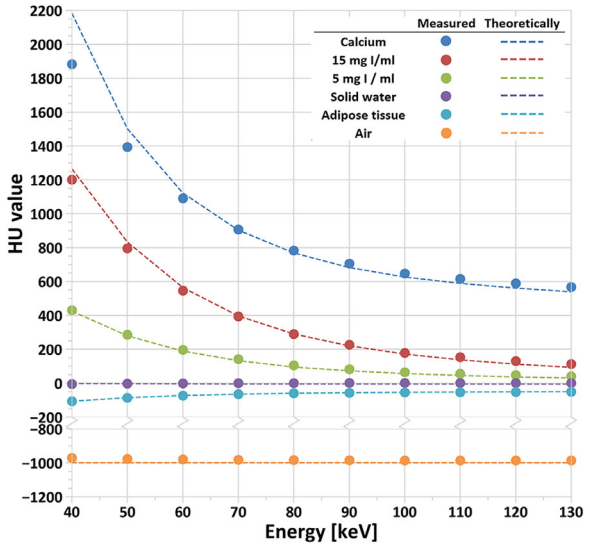

FIGURE 4 Measured and theoretical HU values for 6 rods from 40 to 130 keV in steps of 10 keV. Note: 95% confidence intervals of the measured values are smaller than the size of the marker

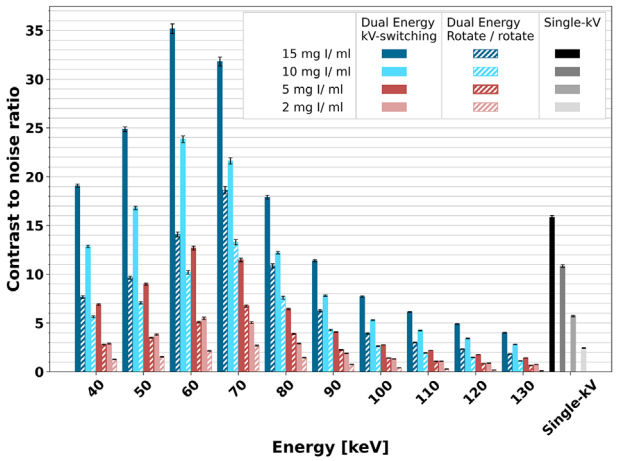

FIGURE 5 Contrast-to-noise ratios (CNRs) of various iodine concentrations versus the energy of the virtual monochromatic images (VMIs) and single-energy reconstructions. DE kV-switching results in higher CNR compared to the DE rotate/rotate method. Error bars indicate 95% confidence intervals

240 mm water phantom, the 320 mm water phantom and the Alderson-Rando phantom were used for this comparison, as they have an attenuation that is closer to the attenuation of a human abdomen than the other phantoms. Also, the dose for the single-kV acquisition is determined with the same SD setting as the DE (SD = 9).

3 | RESULTS

3.1 | CT number and CNR

Figure 4 shows the expected and measured CT numbers. The median absolute difference is 13 HU, with a range of 0 HU (15 mg I/ml at 80 keV) to 300 HU (300 mg Ca/ml at 40 keV). In the supplemental material, a table is given that gives these values in a numerical format including the 95% confidence intervals (table S1). The CNRs for iodine versus water are shown in Figure 5. This figure shows that iodine CNR is higher in VMIs up to 80 keV compared to the single-energy acquisition, and the highest CNR is reached at 60 keV. For the non-iodine rods, the CNR of the kV-switching DE is higher for 60–80 keV compared to that in the single-kV. The highest CNR is reached at 70 keV. The table with all numbers is shown in the supplemental material, Table S2. All CNRs, iodine and non-iodine, of the DE kV-switching method are higher compared to the DE rotate/rotate method.

3.2 | Resolution

The contrasts of the Teflon and LDPE rods using the single-kV reconstruction are 805 HU and 187 HU, respectively. The full TTFs are shown in Figure 6. For each VMI using kV-switching, the TTF for the LDPE rod is lower than that for the Teflon rod. Additionally, the TTF tends to drop with lower VMI energy. Figure 7 shows the frequency at which the TTF drops to 20%. The 20% TTF frequency for the LDPE rod is always higher for the kV-switching DE than for single-kV, however, for the LDPE rod, the TTF of the kV-switching DE is equivalent or higher for VMIs with an energy of 70 keV and above. For the DE rotate/rotate method, the TTFs for both contrasts and all energies are always lower than that for the singe-kV reconstruction.

3.3 | Noise magnitude and noise texture

Figure 8 shows that the noise magnitude is lowest for the 70 keV VMI and highest for the 40 keV VMI. Noticeably, the noise magnitude is comparable in the 320 mm water phantom to that in the 240 mm water phantom, while the same $CTDI_{vol}$ was used. The NPS of the VMI with the lowest SD (70 keV) is shown in Figure 9, along with the NPS of the single-kV acquisition. The NPS for each VMI is provided in the supplementary material (Figure S1). From the average NPS frequency, also shown in Figure 9, it can be seen that the NPSs of the VMIs of the 240 mm water phantom show more power in the higher frequencies than the VMIs of the 320 mm water phantom. From 40 to 60 keV the average frequency drops, while in VMIs with higher energies it rises again. This will change the grain of the noise in the images going over the various VMIs, while for the DE rotate/rotate reconstruction the NPS shape remains constant. The average NPS frequency for each VMI is comparable or higher than the average NPS frequency of the single-kV reconstruction.

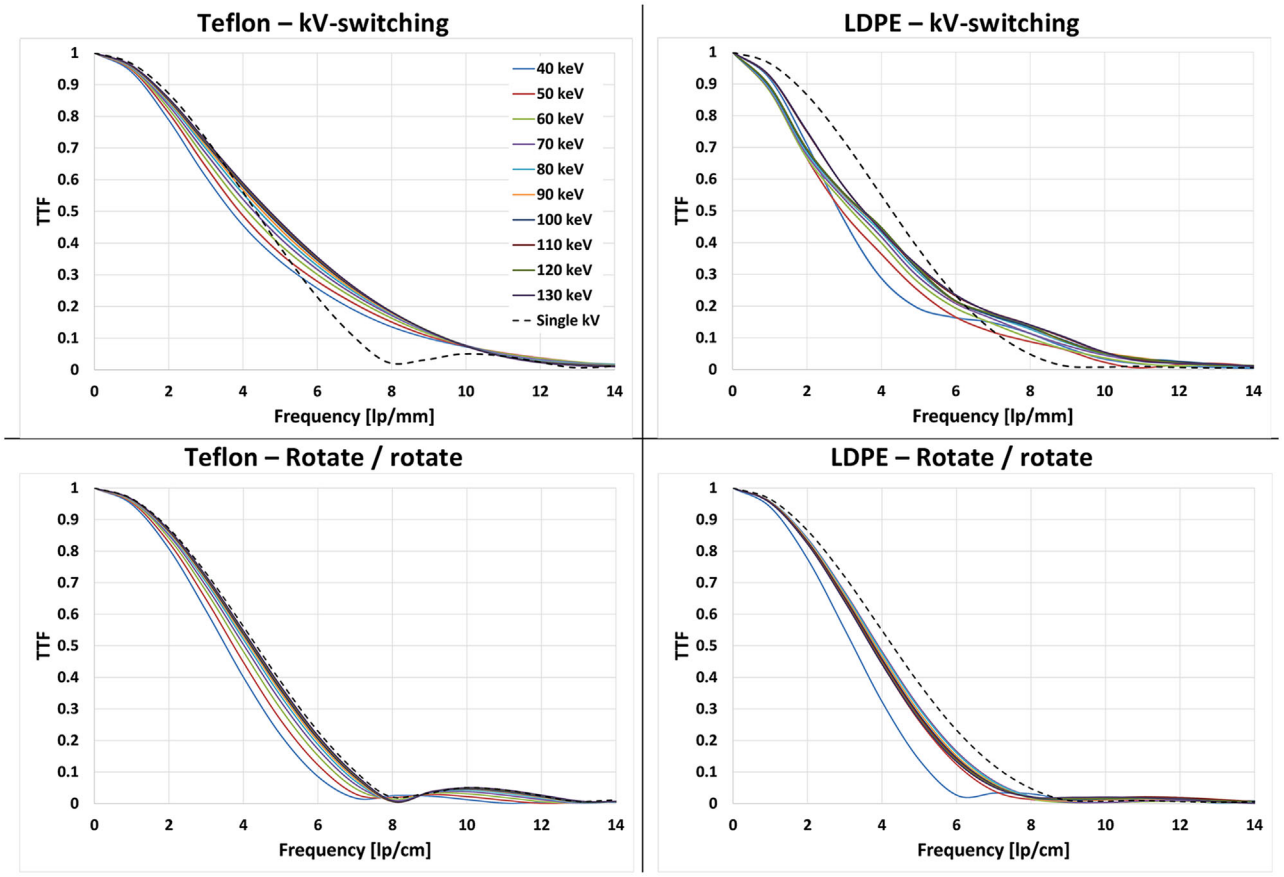

FIGURE 6 Task transfer functions (TTFs) for the DE kV-switching (upper row), and the DE rotate/rotate (lower row) methods for two contrasts: Teflon and LDPE. The TTFs for the single-kV are shown for reference

FIGURE 7 Frequency at which the TTF reaches 20% for each VMI for two contrast levels, as given by Teflon (contrast for single-kV: 805 HU) and LDPE (contrast for single-kV: 187 HU) inserts

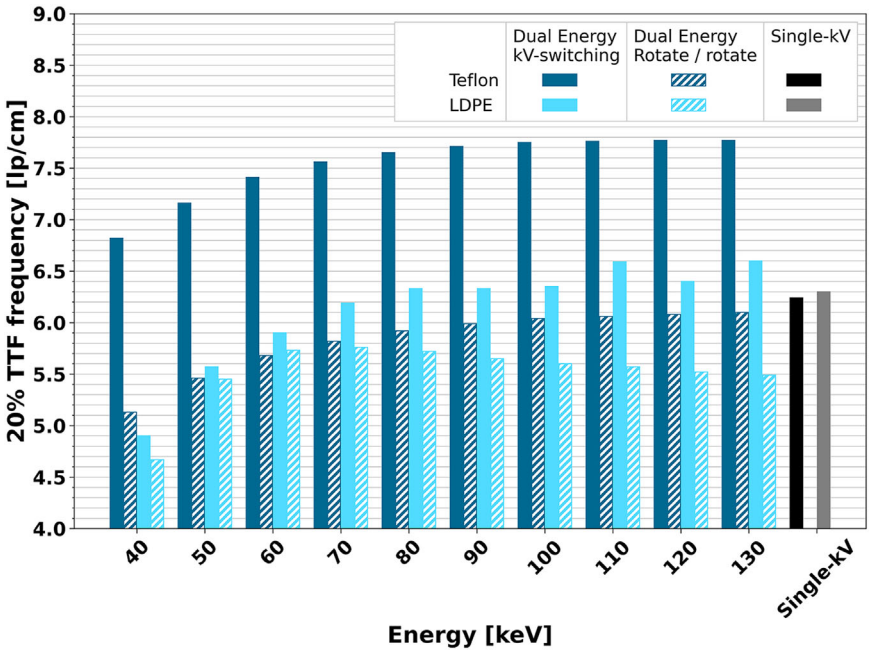

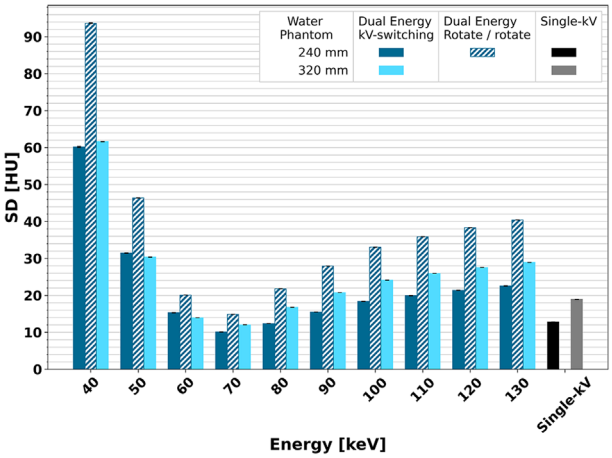

FIGURE 8 Standard deviation as a measure of noise magnitude in a centered ROI in the 240 and 320 mm water phantom for the various VMIs and the single kV reconstruction. Error bars indicate 95% confidence intervals

TABLE 2 Average and standard deviation of the measured iodine concentrations and the differences of the means from the real iodine concentrations

Iodine concentration [mg/ml]	Measured iodine concentration [mg/ml]	Difference	
		[mg/ml]	[%]
2	2.3 ± 0.1	0.3	15
5	5.8 ± 0.3	0.8	16
10	10.9 ± 0.3	0.9	9.0
15	16.1 ± 0.3	1.1	7.3

3.4 | Iodine quantification

The iodine concentrations deviate from their specifications by a maximum of 1.1 mg I/ml (at 15 mg I/ml), while in relative terms the maximum error is 16% (at 5 mg I/ml), see Table 2 for the results of the kV-Switching DECT. The rotate/rotate DECT does not include the option to quantify the iodine content.

3.5 | Low contrast visibility

The low contrast visibility was perceived to be best for the 70 keV VMI in DE mode and comparable to the low contrast visibility of the single-kV image (see Figure 10 and Table 3). The low contrast visibility diminishes for VMIs with an energy below 70 keV. The low contrast visibility of the DE rotate/rotate is lower compared to that in both single-kV and the kV-switching DE images.

3.6 | Artifacts

A slice of the Alderson Rando phantom acquisitions presenting beam hardening artifacts is shown in Figure 11.

TABLE 3 Number of visible contrast objects for each VMI for the kV-switching DE, the DE rotate / rotate in brackets, and for the single-kV reconstruction for the supra-slice as well as the sub-slice contrast objects, as determined by a single reader

VMI [keV]	Supra-slice Contrast [%]			Sub-slice z-axis length [mm]		
	1.0	0.5	0.3	7	5	3
40	2 (1)	1 (0)	0 (0)	0 (0)	0 (0)	0 (0)
50	3 (3)	3 (1)	1 (0)	1 (1)	0 (0)	0 (0)
60	7 (8)	4 (7)	4 (2)	3 (3)	2 (2)	1 (0)
70	8 (7)	7 (5)	6 (2)	3 (2)	3 (2)	3 (0)
80	8 (6)	7 (3)	5 (1)	3 (1)	3 (1)	3 (0)
90	8 (4)	6 (1)	2 (1)	3 (1)	2 (0)	1 (0)
100	8 (3)	5 (0)	0 (0)	3 (0)	2 (0)	0 (0)
110	8 (2)	5 (0)	0 (0)	2 (0)	2 (0)	0 (0)
120	8 (2)	5 (0)	1 (0)	3 (0)	2 (0)	0 (0)
130	8 (1)	5 (0)	1 (0)	2 (0)	2 (0)	0 (0)
Single-kV	9	7	5	3	3	2

It shows that the beam hardening artifact is more pronounced at lower energies. For all VMIs the AI is higher than for the single kV scan. Images of the water phantoms with three additional attenuating objects are shown in Figures 12 and 13. The HU values of the highest-attenuating portions of the objects added to the FOV are approximately 230 HU (the two homogeneous plastic bars at the top of the phantom) and 560 HU (resulting from a hand phantom at the bottom right of the phantom). It can be seen that the images of the 70 keV VMI have more streaks, as well as hypo- and hyperdense blotches compared to the single-kV images for the images with a WED of 28.8 cm (with simulated arms down), and 41.0 cm. It should be noted that the differences in visibility of the artifacts may be impacted by the difference in noise texture and magnitude between DE and single-kV.

3.7 | Dose comparison

The resulting $CTDI_{vol}$ based on the settings for the ATCM advised by the manufacturer are shown for the DE and single-kV modes (SD = 9 for DE, SD = 12.5 for single-kV) in Table 4. Also, the $CTDI_{vol}$ for the single-KV mode with the same SD-setting as the DE mode are given.

4 | DISCUSSION

In this study, we evaluated the technical characteristics of a rapid tube-voltage switching dual energy CT system that uses a deep-learning approach to complete the sinogram data. We found that HU values for

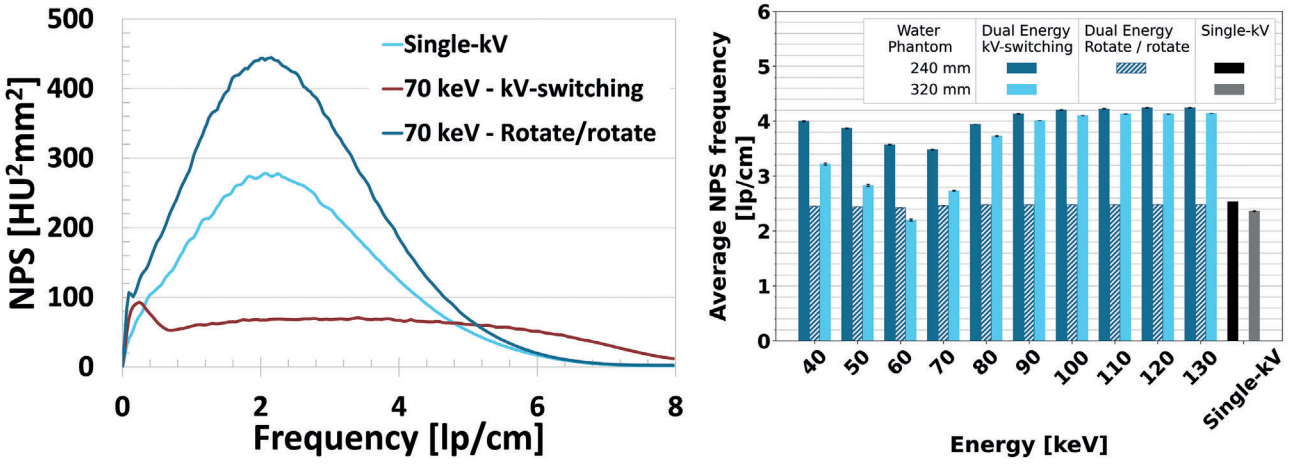

FIGURE 9 Radial profile of the 2D NPSs of the VMIs at 60 and 70 keV and single-kV reconstruction (left) for the 240 mm water phantom and the average frequencies for the NPSs of all VMIs and the single-kV (right). Error bars indicate 95% confidence intervals

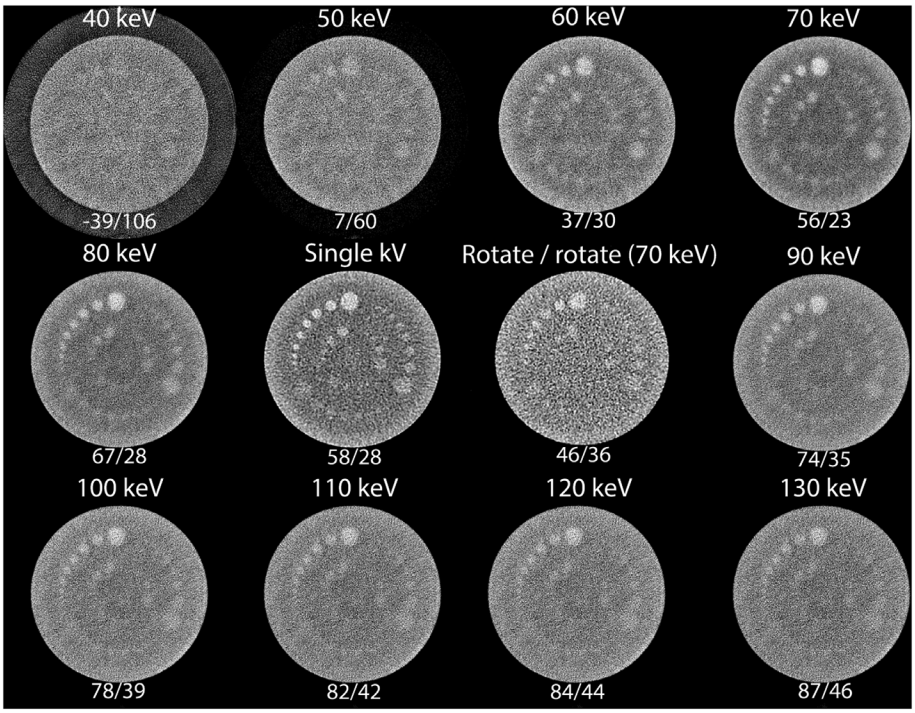

FIGURE 10 Reconstructed 10 mm thick images of the low contrast module of the Catphan 500 for dual energy VMIs and single-kV. Window level and window width (numbers below images) were individually set to show the highest number of low contrast objects. For the rotate/rotate system, only the VMI with the best low-contrast visibility (70 keV) is shown

the various VMIs are consistent with the theoretical HU values. CNRs for iodine are higher than for single-kV for VMIs with an energy of 80 keV and lower, and that the iodine quantification is within 16%. For the 70 keV VMI, the resolution is better or equal to that in the single-kV images and the low contrast visibility is comparable. However, using the manufacturer's recommended settings, compared to single-kV acquisitions, this DE technique uses a higher radiation dose and the current implementation is limited to patients with a maximum BMI of 35 kg/m2 to avoid potentially a lack of signal at the detector.

This kV-switching DECT system has been previously described.[16] However, in that study, the acquisition settings used were outside of manufacturer recommendations. This may lead to more pronounced artifacts (streaks, and hypo- and hyper-dense blotches) and to artifacts within the size thresholds given by the manufacturer. Although a limited set of VMIs was used in that study, the NPS shape does align with our results. The trend of the TTF over the VMIs is different, which might be due to the different contrast (acrylic vs. the Teflon and LDPE used in this study) and the different acquisition parameters.

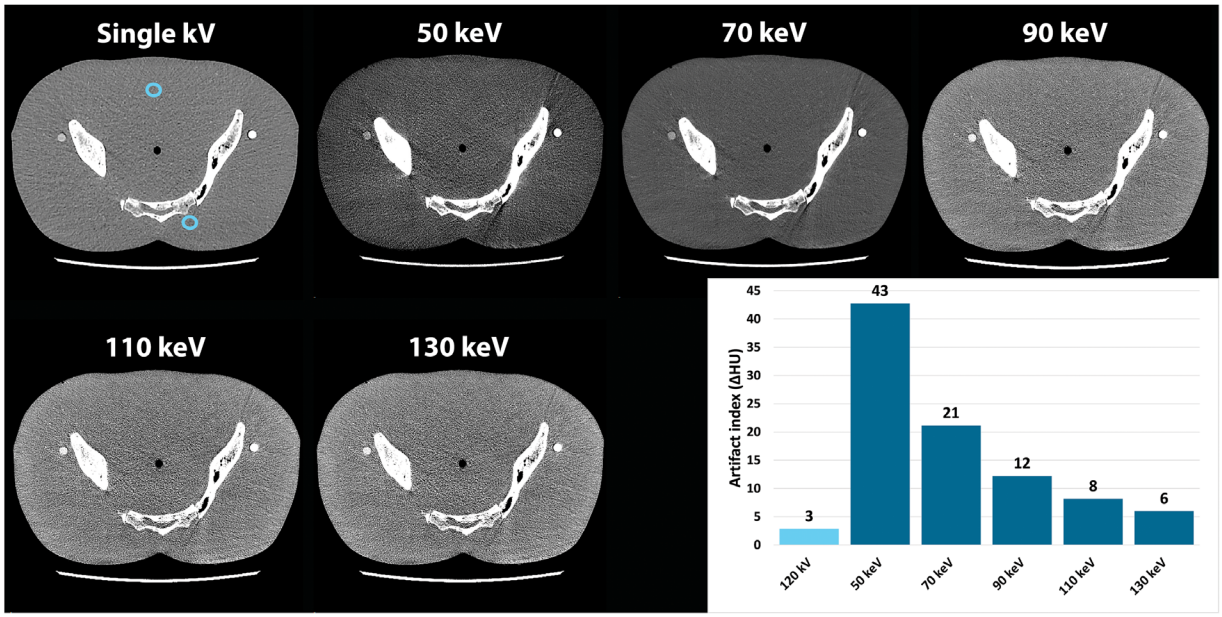

FIGURE 11 Slice containing beam hardening artifacts are shown for the single kV (120 kV) and the virtual mono-energetic images. The absolute HU differences of the mean HU in ROIs within and outside the beam hardening artifact (blue ellipses) are shown in the graph. Window level and Window width are −20 and 200, respectively

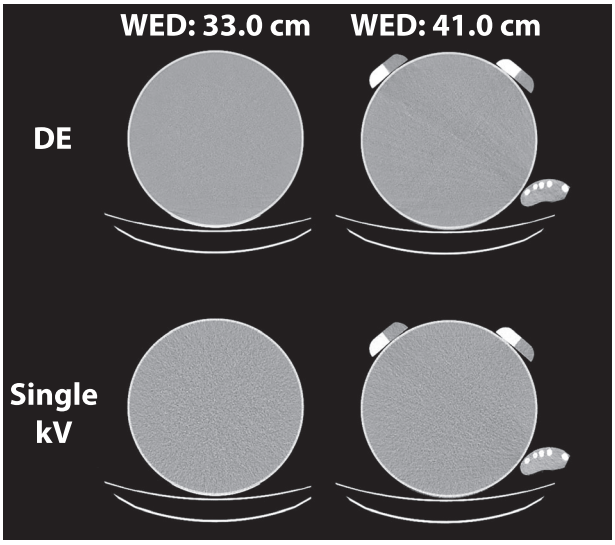

FIGURE 12 Images of acquisitions of a 32 cm diameter water phantom and additional attenuation. Upper row: dual energy (DE) virtual monochromatic images at 70 keV, lower row: 120 kV single-kV images. The DE image with a 41.0 cm water equivalent diameter (WED) clearly contains more artifacts (streaks, and hypo- and hyper-dense blotches) compared to the single-kV image. Window width and level settings are 150 HU and 0 HU, respectively. Note: Differences in noise texture and magnitude between DE and single-kV may impact the visibility of the artifacts

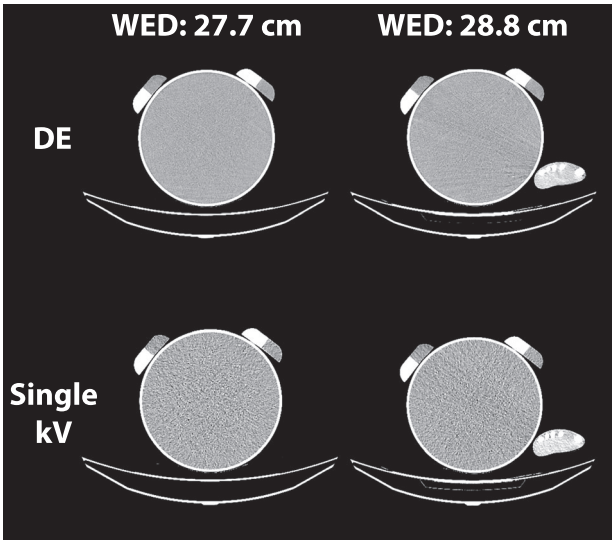

FIGURE 13 Images of acquisitions of a 24 cm diameter water phantom with additional attenuation. Upper row: dual energy (DE) virtual monochromatic images of 70 keV, lower row: 120 kV single-kV images. The DE image with a 28.8 cm water equivalent diameter (WED) clearly contains more artifacts (streaks, and hypo- and hyper-dense blotches) compared to the single-kV images along the high attenuation path. Window width and level settings are 150 HU and 0 HU, respectively. Note: differences in noise texture and noise magnitude between DE and single-kV may impact the visibility of the artifacts

Compared to the performance of other dual energy systems, the results found here demonstrate some unique trends. We found that TTF decrease for VMIs at energies of 80 keV and lower. Greffier et al.[17] reported on four dual energy systems: dual source CT (DSCT, Siemens Somatom Force), split filter CT (SFCT, Siemens Somatom Edge), dual-layer CT (DLCT, Philips IQon Spectral), and fast tube voltage-switching CT (KVCT). According to their results, for all these systems, TTFs increased with lower energy VMIs, while average NPS frequency decreased at VMIs with the lowest energies,

TABLE 4 Volumetric CT dose index ($CTDI_{vol}$) resulting from acquisitions of the phantoms at manufacturer-recommended settings (SD = 9 for DE, SD = 12.5 for single-kV) and at matching noise settings. Due to minimum tube current limitations, the minimum $CTDI_{vol}$ for DE is 12.6 mGy, while for single-kV it is 2.5 mGy (resulting from the minimum tube current of 80 mA)

Phantom	Dual energy (SD = 9) $CTDI_{vol}$ [mGy]	Single-kV (SD = 12.5) $CTDI_{vol}$ [mGy]	Single-kV (SD = 9) $CTDI_{vol}$ [mGy]
240 mm water	12.6	2.5	3.7
320 mm water	12.6	6.0	11.8
Alderson Rando	12.6	2.8	4.0

except for KVCT. That system had the highest average NPS frequency at 70 keV, which then dropped at higher and lower energies. The system studied in this paper has the lowest average peak frequency at 60 keV, which then increases at both higher and lower energies. This behavior might be caused by the reconstruction process leading to the VMIs. The basis material images have different noise texture as a result of the deep-learning based denoising. Since the VMIs are created by the weighted averaging of these basis images, with the weights differing for different energy levels, the noise texture of the VMIs, and therefore the NPS, varies, depending on these weighting coefficients.

The lowest SD values for the DE systems were reached between 60 and 80 keV, as in our study, where the lowest SD was found at 70 keV. For the kV-switching Canon system, the 60 keV VMI has the highest iodine CNR, and the 70 keV VMI has the lowest noise magnitude, while for other systems the highest CNR seems to be at lower energies, except, again, for the KVCT. However, an update has been reported for the KVCT, which suggests that now a higher CNR is obtained at lower energies.[17,18]

Iodine quantification accuracy of this DECT is within 0.3–1.1 mg I/ml for the range from 2 to 15 mg/ml. Using the same phantom, Jacobsen et. al reported DSCT, DLCT, and KVCT to be within 10% for iodine concentrations of 2, 5, and 10 mg I/ml, while the SFCT resulted in a relative error of 35% for the 2 ml I/ml rod.[19] The DECT system investigated here remains within 16% for all tested iodine concentrations.

Theoretically, reconstruction methods for VMIs should be immune from beam hardening.[1,4] However, clinical implementations, especially for VMIs at low energies, do show beam hardening artifacts, as were found for the system investigated here. In addition to beam hardening artifacts in the form of streaks, hyper- and hypo-dense blotches can be seen if a low number of photons reach the detector. This might occur clinically for patients having a BMI above 35 kg/m2 or if additional attenuating material is present in the X-ray beam.

The dose levels used by the system for DE imaging are higher than the values used clinically in our institution for single-kV acquisitions. The main reasons for the higher dose are the lower manufacturer-recommended SD setting (DE: 9 HU, single-kV: 12.5 HU) and the minimum tube current of 230 mA for DE acquisitions. However, the resulting $CTDI_{vol}$ values for the phantoms are comparable to values reported for KVCT. Sugawara et al report a mean $CTDI_{vol}$ level of 12.7 mGy for abdomen for the GE Discovery CT.[20] Purysko et al report a $CTDI_{vol}$ of about 8.7 mGy for abdomen for the Siemens Definition Flash,[21] while Primak et al report a $CTDI_{vol}$ of 15.4 mGy for a 30 cm water phantom to get the same noise level as is clinically used for single-kV.[22]

This study has some limitations. First, the study is performed at only one dose level. This dose level is reached by using the parameters that are recommended by the manufacturer. However, the dose level, or noise level in the projection domain, may affect nonlinear reconstruction algorithms with respect to noise texture and resolution.[14] Also, we only used the abdomen mode and did not use other available organ modes. It is known that such kernels can change noise and resolution properties, however, we hypothesize that the relative effects compared to the corresponding single-kV kernel will remain the same or similar. Finally, results presented here are not generalizable to other DECT systems or may even change with new software implementations on the system characterized here.

5 | CONCLUSIONS

At manufacturer-recommended ATCM settings for abdominal imaging, this DE implementation results in higher $CTDI_{vol}$ compared to single-kV acquisitions. However, it can create sharper, lower noise VMIs with up to 2.5 times higher iodine CNR compared to single-kV images acquired at the same dose.

ACKNOWLEDGMENT

We thank Wouter Veldkamp and Jan Heemskerk from the Leiden University Medical Center for providing access to their Multi-Energy CT phantom. This work was funded by Canon Medical Systems Corporation.

CONFLICT OF INTEREST

Kirsten L. Boedeker and Daniel Shin are employees of Canon Medical Systems Corporation. Christiana Balta is employee of Canon Medical Systems Europe. Mathias Prokop and Ioannis Sechopoulos have research agreements with Canon Medical Systems Corporation.

REFERENCES

1. McCollough CH, Leng S, Yu L, Fletcher JG. Dual- and multi-energy CT: principles, technical approaches, and clinical applications. *Radiology*. 2015;276(3):637-653. doi: 10.1148/radiol.2015142631

2. Euler A, Parakh A, Falkowski AL, et al. Initial results of a single-source dual-energy computed tomography technique using a split-filter: assessment of image quality, radiation dose, and accuracy of dual-energy applications in an in vitro and in vivo study. *Invest Radiol*. 2016;51(8):491-498. doi: 10.1097/RLI.0000000000000257
3. Rajendran K, Petersilka M, Henning A, et al. First clinical photon-counting detector CT system: technical evaluation. *Radiology*. 2022;303(1):130-138. doi: 10.1148/RADIOL.212579
4. Yu L, Leng S, McCollough CH. Dual-energy CT-based monochromatic imaging. *AJR Am J Roentgenol*. 2012;199(5):9-15. doi: 10.2214/ajr.12.9121. Suppl.
5. Akagi M, Nakamura Y, Higaki T, et al. Deep learning reconstruction improves image quality of abdominal ultra-high-resolution CT. *Eur Radiol*. 2019;29(11):6163-6171. doi: 10.1007/s00330-019-06170-3
6. Higaki T, Nakamura Y, Zhou J, et al. Deep learning reconstruction at CT: phantom study of the image characteristics. *Acad Radiol*. 2020;27(1):82-87. doi: 10.1016/j.acra.2019.09.008
7. Park SY, Kim CK, Park BK. Dual-energy CT in assessing therapeutic response to radiofrequency ablation of renal cell carcinomas. *Eur J Radiol*. 2014;83(2):e73-e79. doi: 10.1016/j.ejrad.2013.11.022
8. Meyer M, Hohenberger P, Apfaltrer P, et al. CT-based response assessment of advanced gastrointestinal stromal tumor: dual energy CT provides a more predictive imaging biomarker of clinical benefit than RECIST or Choi criteria. *Eur J Radiol*. 2013;82(6):923-928. doi: 10.1016/j.ejrad.2013.01.006
9. Boll DT, Patil NA, Paulson EK, et al. Renal stone assessment with dual-energy multidetector CT and advanced postprocessing techniques: improved characterization of renal stone composition-pilot study. *Radiology*. 2009;250(3):813-820. doi: 10.1148/radiol.2503080545
10. Marri UK, Das P, Shalimar KalaivaniM, Srivastava DN, Madhusudhan KS. Noninvasive staging of liver fibrosis using 5-minute delayed dual-energy CT: comparison with US elastography and correlation with histologic findings. *Radiology*. 2021;298(3):600-608. doi: 10.1148/radiol.2021202232
11. Nagayama Y, Kato Y, Inoue T, et al. Correction to: liver fibrosis assessment with multiphasic dual-energy CT: diagnostic performance of iodine uptake parameters (European Radiology, (2021), 31, 8, (5779-5790) doi: 10.1007/s00330-021-07706-2 *Eur Radiol*. 2021;31(11):8823-8824. doi: 10.1007/s00330-021-07994-8
12. Xu J, Wang X, Yang P, Luo K, He X. Size-specific dose estimates of radiation based on body weight and body mass index for chest and abdomen-pelvic CTs. *Biomed Res Int*. 2020;2020:1-8. doi: 10.1155/2020/6046501
13. Nute JL, Jacobsen MC, Stefan W, Wei W, Cody DD. Development of a dual-energy computed tomography quality control program: characterization of scanner response and definition of relevant parameters for a fast-kVp switching dual-energy computed tomography system. *Med Phys*. 2018;45(4):1444-1458. doi: 10.1002/mp.12812
14. Richard S, Husarik DB, Yadava G, Murphy SN, Samei E. Towards task-based assessment of CT performance: system and object MTF across different reconstruction algorithms. *Med Phys*. 2012;39(7):4115-4122. doi: 10.1118/1.4725171
15. Boedeker KL, Cooper VN, McNitt-Gray MF. Application of the noise power spectrum in modern diagnostic MDCT: part I. Measurement of noise power spectra and noise equivalent quanta. *Phys Med Biol*. 2007;52(14):4027-4046. doi: 10.1088/0031-9155/52/14/002
16. Greffier J, Si-Mohamed S, Guiu B, et al. Comparison of virtual monoenergetic imaging between a rapid kilovoltage switching dual-energy computed tomography with deep-learning and four dual-energy CTs with iterative reconstruction. *Quant Imaging Med Surg*. 2022;12(2):1149-1162. doi: 10.21037/qims-21-708
17. Greffier J, Si-Mohamed S, Dabli D, et al. Performance of four dual-energy CT platforms for abdominal imaging: a task-based image quality assessment based on phantom data. *Eur Radiol*. 2021;31(7):5324-5334. doi: 10.1007/s00330-020-07671-2
18. Noda Y, Goshima S, Kaga T, et al. Virtual monochromatic image at lower energy level for assessing pancreatic ductal adenocarcinoma in fast kV-switching dual-energy CT. *Clin Radiol*. 2020;75(4):320.e17-320.e23. doi: 10.1016/j.crad.2019.11.012
19. Jacobsen MC, Schellingerhout D, Wood CA, et al. Intermanufacturer comparison of dual-energy CT iodine quantification and monochromatic attenuation: a phantom study. *Radiology*. 2018;287(1):224-234. doi: 10.1148/radiol.2017170896
20. Sugawara H, Takayanagi T, Ishikawa T, et al. New fast kVp switching dual-energy CT: reduced severity of beam hardening artifacts and improved image quality in reduced-iodine virtual monochromatic imaging. *Acad Radiol*. 2020;27(11):1586-1593. doi: 10.1016/j.acra.2019.11.015
21. Purysko AS, Primak AN, Baker ME, et al. Comparison of radiation dose and image quality from single-energy and dual-energy CT examinations in the same patients screened for hepatocellular carcinoma. *Clin Radiol*. 2014;69(12):e538-e544. doi: 10.1016/j.crad.2014.08.021
22. Primak AN, Giraldo JCR, Eusemann CD, et al. Dual-source dual-energy CT with additional tin filtration: dose and image quality evaluation in phantoms and in vivo. *Am J Roentgenol*. 2010;195(5):1164-1174. doi: 10.2214/AJR.09.3956

SUPPORTING INFORMATION

Additional supporting information can be found online in the Supporting Information section at the end of this article.

How to cite this article: Oostveen LJ, Boedeker KL, Balta C, et al. Technical performance of a dual-energy CT system with a novel deep-learning based reconstruction process: Evaluation using an abdomen protocol. *Med Phys*. 2022;1-12. https://doi.org/10.1002/mp.16151